RESEARCH ARTICLE

MEMBRANES

Truly combining the advantages of polymeric and zeolite membranes for gas separations

Xiaoyu Tan[1], Sven Robijns[2], Raymond Thür[1]†, Quanli Ke[2]‡, Niels De Witte[3], Aran Lamaire[4], Yun Li[1], Imran Aslam[1], Daan Van Havere[1], Thibaut Donckels[2], Tom Van Assche[3], Veronique Van Speybroeck[4], Michiel Dusselier[2]*, Ivo Vankelecom[1]*

Mixed-matrix membranes (MMMs) have been investigated to render energy-intensive separations more efficiently by combining the selectivity and permeability performance, robustness, and nonaging properties of the filler with the easy processing, handling, and scaling up of the polymer. However, truly combining all in one single material has proven very challenging. In this work, we filled a commercial polyimide with ultrahigh loadings of a high–aspect ratio, CO_2-philic Na-SSZ-39 zeolite with a three-dimensional channel system that precisely separates gas molecules. By carefully designing both zeolite and MMM synthesis, we created a gas-percolation highway across a flexible and aging-resistant (more than 1 year) membrane. The combination of a CO_2-CH_4 mixed-gas selectivity of ~423 and a CO_2 permeability of ~8300 Barrer outperformed all existing polymer-based membranes and even most zeolite-only membranes.

Over the past decades, membrane technology has matured into an established technology for many energy-intensive separations (*1*–*3*). Compared with conventional technologies, membrane technology offers a more sustainable alternative, owing to its low energy consumption, small footprint, and modular design, making it possible to retrofit membranes in existing plants (*2*, *3*). Membranes are already in use for gas separations—for example, natural gas purification, syngas treatment, and air separation (*4*–*7*)—and are becoming part of the toolbox for CO_2 removal (*5*–*10*). Whereas conventional polymeric membranes are cheap and processable, they often suffer from aging issues or an intrinsic permeability-selectivity trade-off, which makes it challenging to obtain high permeability together with sufficient selectivity (*11*–*16*). On the other hand, inorganic membranes prepared from zeolites or other crystalline microporous materials, such as metal-organic frameworks (MOFs), typically display better separation performances but tend to be brittle and more expensive and possess poor processability and scalability (*17*–*21*). Mixed-matrix membranes (MMMs), which consist of fillers embedded in a polymeric matrix, aim at combining the intrinsic advantages of a polymeric membrane with the filler's superior gas separation properties (*22*–*27*).

Zeolites are of particular interest for MMM development because they have well-defined, rigid pores and outstanding thermal and chemical stability. Because the intrinsically low selectivity and high permeability of rubbery polymers (such as polydimethylsiloxane) neutralize the benefits of the zeolite, rigid glassy polymers are key for the development of high-performance zeolite-filled MMMs (*28*–*32*). However, the poor adhesion between zeolites and glassy polymers typically results in nonselective interfacial voids (*31*, *32*). Consequently, obtaining high zeolite loadings (≥50 wt %) while guaranteeing a defect-free polymer-zeolite interface in combination with a highly selective zeolite and appropriate glassy polymer matrix is essential to the creation of high-performance MMMs for a variety of the most critical separation challenges. In this work, a platelet-shaped, CO_2-philic, small-pore (eight-membered ring) AEI-type zeolite (SSZ-39) (*33*–*36*), possessing a long-range ordered three-dimensional (3D)–channel system and gas-selective windows, was incorporated in a poly(3,3′-4,4′-benzophenone tetracarboxylic-dianhydride diaminophenylindane) (Matrimid 5218) polymer. Because of the combination of well-designed zeolite and MMM syntheses, we obtained a high zeolite loading with a quasi-continuous zeolite phase across a self-standing membrane.

Result and discussion

Zeolite characterization

SSZ-39 zeolites were synthesized according to modified literature recipes (*33*–*35*). X-ray diffraction (XRD) of the samples confirmed the highly crystalline, pure AEI type zeolite (fig. S9). N_2 physisorption demonstrated a micropore volume of ~0.3 cm^3/g (fig. S11), which is close to the theoretical accessible volume of the AEI framework (*37*), suggesting a nearly perfect 3D-connected channel system, which allows fast gas transport. Transmission electron microscopy (TEM) images showed platelet-shaped SSZ-39 particles (Fig. 1A) of ~150 nm thickness and ~1.8 by 1.8 μm in size (fig. S48), the average aspect ratio thus reaching ~12. The random packing of the high–aspect ratio zeolite platelets (fig. S49) results in a low bulk density of ~15 mg/cm^3 (fig. S12), and elemental analysis of the as-synthesized SSZ-39 indicated a Si/Al molar ratio of ~11 (table S3).

CO_2, CH_4, and N_2 uptake and isosteric adsorption enthalpies (Q_{st}) were determined for both calcined SSZ-39 (Na/Al ratio ≈ 0.12) and Na^+-exchanged SSZ-39 (Na-SSZ-39; Na/Al ratio ≈ 0.93) (table S3). The adsorption isotherms of CO_2, CH_4, and N_2 at 10°C are shown in Fig. 1D for a pressure range of 0 to 8 bar. The theoretical maximum CO_2 uptake of Na-SSZ-39 reached ~7.0 mmol/g (~11.0 $mmol/cm^3$) at 10°C, and the steric heat of adsorption for CO_2 at zero coverage was −35.1 kJ/mol, reflecting a desired strong physical adsorption for membrane applications. For both SSZ-39 and Na-SSZ-39, the gas uptake decreases in the order $CO_2 \gg CH_4 > N_2$. The isosteric adsorption enthalpy of CO_2 in Na-SSZ-39 was far larger than that of CH_4 (−21.4 kJ/mol) and N_2 (−19.4 kJ/mol) as a result of the large polarizability and quadrupole moment of CO_2 (*38*). A more negative CO_2 adsorption enthalpy was obtained on Na-SSZ-39 compared with SSZ-39 (table S19). Additionally, the pronounced difference in CO_2 adsorption in the low-pressure region of the isotherms (Fig. 1D) suggests that Na^+ exchange resulted in an increased CO_2-philicity (*38*).

To better understand these findings at a molecular level, the pure-gas and mixed-gas adsorption behaviors in Na-SSZ-39 were modeled by using grand canonical Monte Carlo (GCMC) simulations. The pure-gas adsorption simulations show a good qualitative resemblance with the experimental data (fig. S37), and the enthalpies of adsorption are in good agreement (at 2 bar, GCMC yields −31.6 kJ/mol for CO_2, −18.5 kJ/mol for CH_4, and −15.8 kJ/mol for N_2). The 3D density isosurfaces for CO_2 adsorption (Fig. 1C) show that CO_2 molecules preferentially interact with the Na^+ (especially at low CO_2 pressures), whereas the windows of Na-SSZ-39 remain open for gas transport. This tendency corroborates the enhanced CO_2-philicity through Na^+ exchange, improving CO_2 adsorption and transport in Na-SSZ-39. The Si/Al molar ratio of 11 implies that on average, one aluminum site (fully counted) and thus one sodium ion exists per cage (*37*). Furthermore,

[1]Centre for Membrane Separations, Adsorption, Catalysis and Spectroscopy for Sustainable Solutions (cMACS), KU Leuven, Celestijnenlaan 200F, 3001 Leuven, Belgium. [2]Center for Sustainable Catalysis and Engineering, KU Leuven, Celestijnenlaan 200F, 3001 Leuven, Belgium. [3]Department of Chemical Engineering, Vrije Universiteit Brussel, Pleinlaan 2, 1050 Brussels, Belgium. [4]Center for Molecular Modeling, Ghent University, Tech Lane Ghent Science Park, Technologiepark 46, 9052 Zwijnaarde, Belgium.
*Corresponding author. Email: ivo.vankelecom@kuleuven.be (I.V.); michiel.dusselier@kuleuven.be (M.D.)
†Present address: Agfa-Gevaert NV, Septestraat 27, 2640 Mortsel, Belgium.
‡Present address: Institute of Catalytic Reaction Engineering, Zhejiang University of Technology, Hangzhou 310014, China.

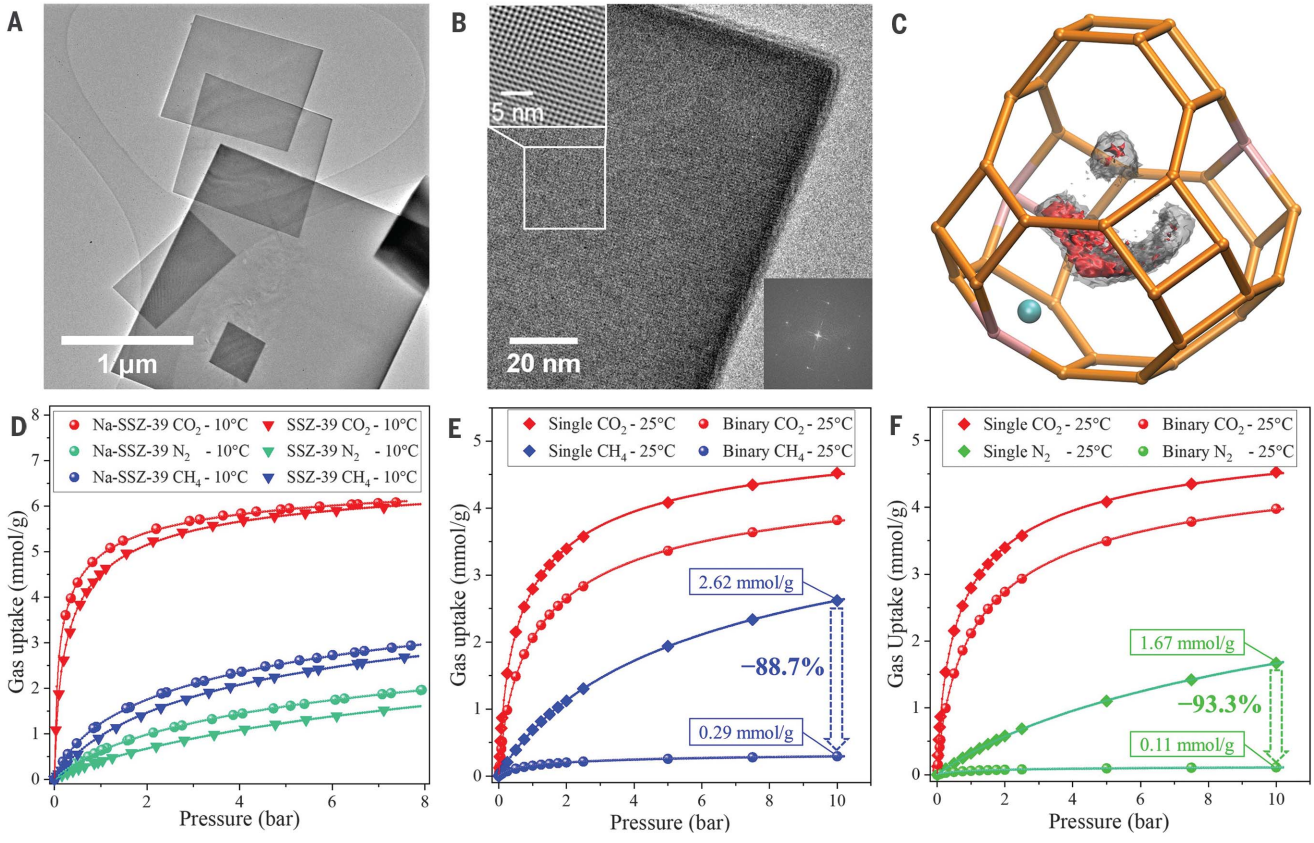

Fig. 1. SSZ-39 zeolite. (**A** and **B**). TEM images of (A) Na-SSZ-39 platelet and (B) its base-face. (Insets) (top left) A Fourier-filtered image from the selected area and (bottom right) the Fourier-transform of this image, proving that the base face refers to the [001] crystal plane of the AEI-type framework (fig. S47). (**C**) 3D density isosurface for CO_2 adsorption in a Na-SSZ-39 cage at 0.1 bar (red) and 1 bar (gray) under 25°C [by means of GCMC, where (3 × 1/3) Al sites are pink, Na^+ is cyan, and O is omitted], indicating that the Na^+ is a preferential adsorption site, particularly at lower pressures. At higher pressures, additional molecules are adsorbed, occupying the remaining space of the cage. (**D**) Experimental CO_2, CH_4, and N_2 adsorption isotherms of SZZ-39 and Na-SSZ-39 zeolites at 10°C. (**E**) Single-gas and equimolar mixed-gas CO_2-CH_4 adsorption isotherms of Na-SSZ-39 zeolite at 25°C (by means of GCMC). (**F**) Single-gas and equimolar mixed-gas CO_2-N_2 adsorption isotherms of Na-SSZ-39 zeolite at 25°C (by means of GCMC) (supplementary materials).

the CO_2-CH_4 and CO_2-N_2 mixed-gas sorption simulations demonstrate the competitive sorption of CO_2 at the expense of CH_4 and N_2 (movie S1). This strong competitive sorption behavior drastically reduces the uptake of CH_4 and N_2. For example, compared with the single-gas adsorption, the CH_4 uptake from an equimolar CO_2-CH_4 mixture was reduced by 88.7% (for N_2, 93.3%) at 10 bar/25°C (Fig. 1, E and F). In addition, ab initio free-energy barrier calculations [by using enhanced sampling molecular dynamics (MD) simulations] for the diffusion inside the zeolite confirmed the molecular sieving behavior of Na-SSZ-39 (fig. S41). The biggest (static) aperture of Na-SSZ-39 predicts diffusion of molecules with a diameter of 3.84 Å, which is close to the kinetic diameter of CH_4 (3.80 Å) but prominently larger than that of CO_2 (3.30 Å). Consequently, the free-energy barrier for CH_4 permeation through the eight-membered ring in Na-SSZ-39 is far higher than for CO_2 (a 18.7 kJ/mol difference). Therefore, the self-diffusion coefficient for CO_2 is ~1000-fold greater than for CH_4. Consequently, in a CO_2-CH_4 mixture, CH_4 is prevented from entering the zeolite by a geometric restriction supplemented by a competitive advantage in CO_2 adsorption. By combining the results of MD and GCMC simulations, the theoretical equimolar CO_2-CH_4 mixed-gas selectivity in Na-SSZ-39 zeolite mounted to >10,000 (at 25°C), thus pointing toward a substantial potential for further improving membrane performance on the basis of this zeolite platform (supplementary materials).

MMM characterization

Self-standing MMMs were prepared, with Na-SSZ-39 reaching extremely high loadings of up to 55 wt %. XRD confirmed the preservation of zeolite crystallinity in MMMs after all synthesis steps (fig. S13). Scanning electron microscopy (SEM) membrane cross sections (Fig. 2A) show that the zeolite platelets are positioned in the polymer matrix in a random, nonaligned packing. This homogeneous distribution of zeolite platelets at high loading was realized through a subtle and carefully optimized interplay between zeolite and casting solution during MMM synthesis. More specifically, favorable molecular interactions between zeolite and the Matrimid-chloroform solution were combined with a small density difference between zeolite and solvent (~1.55 g/cm^3 and ~1.49 g/cm^3, respectively), the high–aspect ratio of the filler, a high viscosity of the casting solution, dedicated evaporation control of the solvent, and thermal annealing. After membrane solidification, remaining interfacial defects were eliminated by means of a tuned annealing protocol, which had a profound impact on the final MMM performance (fig. S59). The 180°C annealing program resulted in slightly more permeable membranes than those of the 260°C program, but the 260°C program induced a far higher CO_2-CH_4 selectivity [for 50 wt % Na-SSZ-39 MMM, the selectivity increased from ~200 to >420 (table S5)], whereas the 350°C program resulted in fragile and brittle

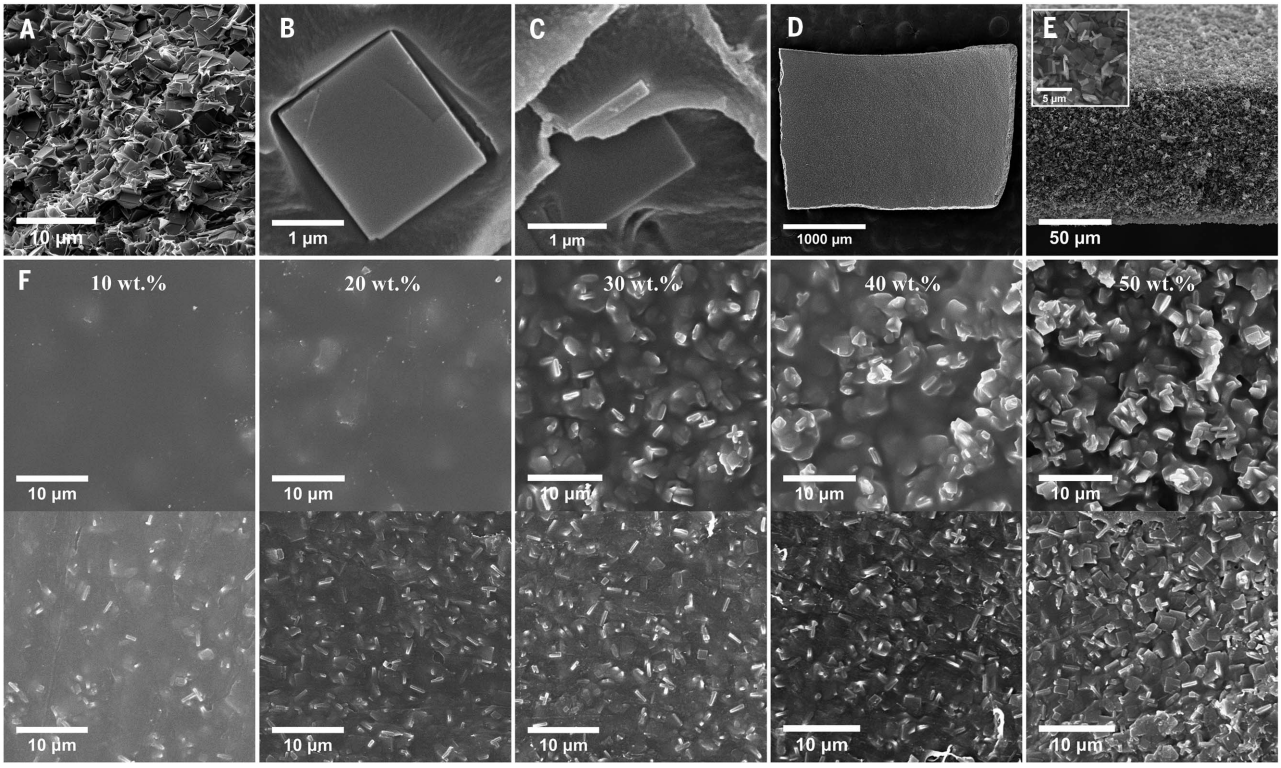

Fig. 2. SEM images of the platelet-shaped Na-SSZ-39 MMMs. (**A**) Cross section of the 40 wt % Na-SSZ-39 MMM after 260°C annealing. (**B** and **C**) Cross section of 20 wt % Na-SSZ-39 MMM (B) before and (C) after annealing. (**D**) Top view and (**E**) cross section of the 30 wt % Na-SSZ-39 MMM after 800°C oxidative treatment, burning off the polymer (figs. S51 to S53). (**F**) (Top) Top view and (bottom) bottom view of membranes with 10 to 50 wt % platelet-shaped zeolite loading (supplementary materials).

carbonized membranes. As shown in Fig. 2C, 260°C-annealed membranes did not show sieve-in-a-cage morphology, which traditionally is a major issue for zeolite MMMs (*31*). Compared with its nonannealed counterparts (Fig. 2B), a much better zeolite-polymer adhesion can be observed (figs. S54 and S55). Full removal of the polymer by means of oxidative treatment at 800°C (fig. S51) led to a stable zeolite-only film (Fig. 2, D and E, and figs. S51 to S53), confirming the high zeolite loading in a random packing. This nearly continuous zeolite phase across the MMM thus creates a "percolation highway" to allow ultrafast permeation of the selected gas molecules.

As anticipated, neither Fourier transform infrared nor Raman microspectroscopy could find evidence for a covalent interaction between polymer and zeolite after annealing (figs. S18 and S61 to S66). Differential scanning calorimetry analysis indicated very good polymer-zeolite interactions in the MMM: With the Na-SSZ-39 loading, the glass transition temperature increased from 314°C (for Matrimid) to 325°C (for annealed Na-SSZ-39 MMMs), pointing toward "wrapping" of the zeolite by the polymer and rigidification of the polymer chains at the interface (fig. S17). We performed CO_2, CH_4, and N_2 sorption experiments on the 260°C annealed Matrimid membrane and the 50 wt % Na-SSZ-39 MMM to quantify their respective gas uptake. A substantially higher gas uptake was noted for the MMM (fig. S30).

Membrane gas separation performance

The mixed-gas selectivities of Na-SSZ-39 MMMs (table S5) were clearly higher than those of their ideal-gas selectivities (table S8) because of the competitive sorption of CO_2 in the Na-SSZ-39 zeolite. For example, for the 50 wt % Na-SSZ-39 MMM, the CO_2-CH_4 ideal-gas selectivity was ~336 (1 bar/25°C), whereas the equimolar CO_2-CH_4 mixed-gas selectivity reached >420 (2 bar/25°C—1 bar CO_2 and CH_4 partial pressures). Likewise, the CO_2-N_2 ideal-gas selectivity at 1 bar/25°C was ~32, whereas its mixed-gas selectivity at 2 bar/25°C increased to ~60. Once the stronger adsorbing CO_2 occupied the adsorption sites, the zeolite channels become partly inaccessible for the other gas, thus inhibiting permeation of CH_4 and N_2.

On the basis of the physisorption and ideal-gas permeation results, gas solubility and diffusivity values were calculated for the unfilled Matrimid membrane and 50 wt % Na-SSZ-39 MMM (table S20). With respect to the unfilled membrane, the MMM displayed a 4.6-times greater CO_2 solubility, whereas the CH_4 and N_2 solubility increased by 7.5 and 3.4 times, respectively. A 220-fold increase in CO_2 diffusivity was denoted for the MMM compared with that of the unfilled Matrimid membrane, whereas CH_4 and N_2 diffusivity only increased 14 and 148 times, respectively. The enhancement of CO_2-CH_4 diffusivity selectivity thus explains the strong improvement of the MMM gas separation capability (table S21). This results from the sharp size-sieving effect of Na-SSZ-39 for the CO_2-CH_4 pair. The increase in diffusivity selectivity for CO_2-N_2 is less pronounced because N_2 possesses a smaller kinetic diameter. The notable difference in separation factor for CO_2-CH_4 and CO_2-N_2 confirms the central role of the highly accurate size-sieving mechanism for the strong selectivities of Na-SSZ-39 MMMs.

Mixed-gas CO_2-CH_4 and CO_2-N_2 separation performances are presented in Fig. 3. For CO_2-CH_4, we observed a continuous increase in separation factor with increasing Na-SSZ-39 loading. Whereas the unfilled Matrimid membrane denotes a CO_2-CH_4 separation factor of ~45 and CO_2 permeability ~8 Barrer, we obtained the best MMM performance with the 50 wt % Na-SSZ-39 loading, which obtained a selectivity of >420 at 2 bar/25°C (~10-fold increase) at a simultaneous extreme CO_2 permeability of ~8280 Barrer (~1037-fold increase). We obtained similar results for the CO_2-N_2 separation performance in which the 50 wt %

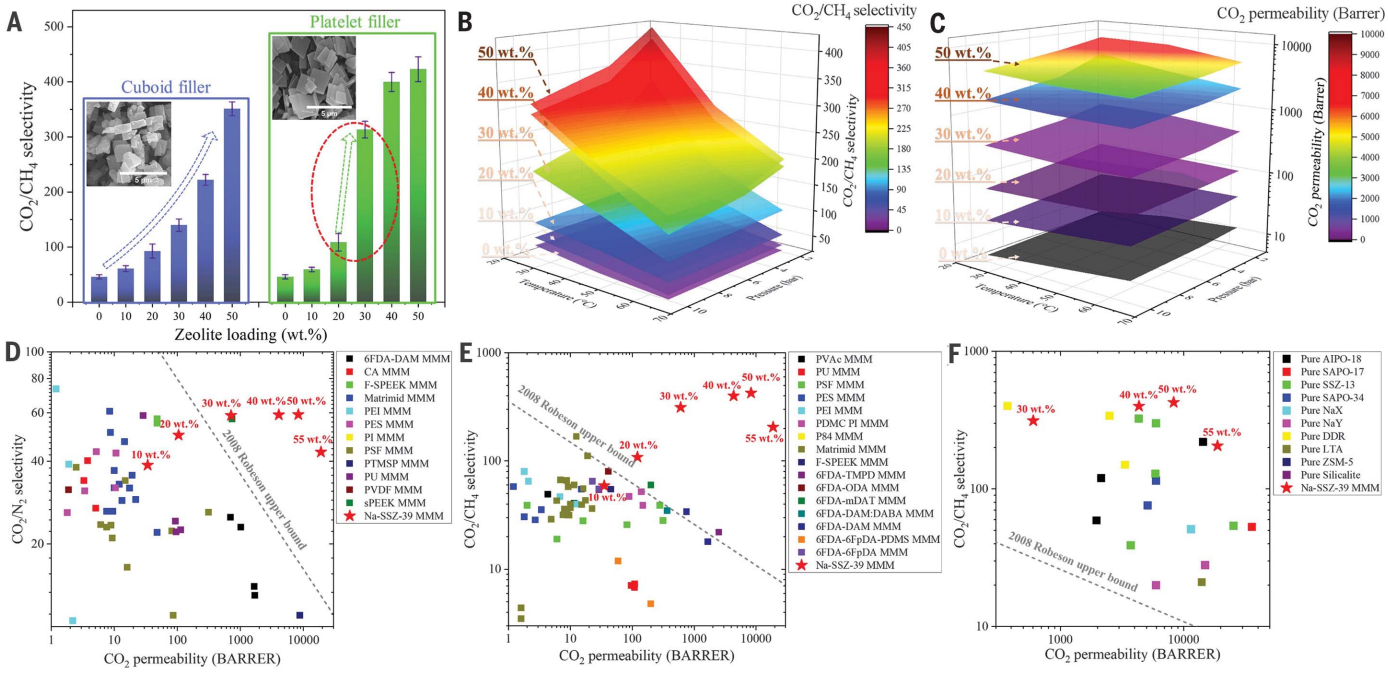

Fig. 3. The gas separation performances of Na-SSZ-39 MMMs. (**A**) The selectivity difference between cuboid-shaped and platelet-shaped Na-SSZ-39 MMMs. (Inset) SEM images show the morphology difference of two zeolites. (**B** and **C**) The temperature and pressure dependence of CO_2-CH_4 selectivity and CO_2 permeability. Nine points constitute a plane. (**D** and **E**) The performance of zeolite-filled MMMs from literature are shown in CO_2-N_2 and CO_2-CH_4 2008 Robeson plots. The red stars indicate the platelet-shaped Na-SSZ-39 MMMs. (**F**) The pure zeolite membranes from literature compared with the Na-SSZ-39 MMMs (≥30 wt %) and 2008 CO_2-CH_4 Robeson plot (full datasets are available in the supplementary materials).

MMM combined a CO_2 permeability of >8300 Barrer with a CO_2-N_2 separation factor of ~60 (versus ~8 and ~35 for unfilled Matrimid). The temperature and pressure dependency of the membrane performance are shown in Fig. 3, B and C, with different zeolite loadings. With increasing temperature, the CO_2 adsorption in the zeolite obviously decreased (fig. S27), resulting in lowered CO_2 permeability and CO_2-CH_4 selectivity. We observed similar behavior with rising feed pressure: Both CO_2 permeability and CO_2-CH_4 selectivity reduced. Because of its high CO_2-philicity, Na-SSZ-39 is already saturated with CO_2 molecules at low feed pressure. Further increased pressures thus contribute less to CO_2 permeation. For the same reason, the Na-SSZ-39 MMMs exhibit enhanced performance in feeds with lower CO_2 partial pressures (table S6). For example, the 50 wt % Na-SSZ-39 MMM gave a CO_2 permeability of >10,000 Barrer and a CO_2-CH_4 selectivity >460 for a 20 vol % CO_2/80 vol % CH_4 feed (figs. S23 and S24), which is close to the compositions of industrial feed streams, such as certain biogas and natural gas sources (*39*, *40*).

When depicted on selectivity-permeability trade-off plots, the Na-SSZ-39 MMMs already surpass the 2008 Robeson upper bound (*11*) from 30 wt % loading onward for CO_2-N_2 (Fig. 3D) and even from 20 wt % for CO_2-CH_4 (Fig. 3E). Ultimately, they realize an unprecedented jump toward the upper-right corner of the Robeson plot, ending up even beyond the performance area that is dominated by zeolite-only membranes (Fig. 3F). Outperforming most existing zeolite-only membranes can be related to the properties of the Na-SSZ-39 filler as well as the membrane morphology. Moreover, compared with the zeolite-only membranes, the Na-SSZ-39 MMMs (Fig. 4B) additionally keep their flexibility because of the presence of the polymer matrix (Fig. 4A and movie S2). Furthermore, because of the stability of the Na-SSZ-39 filler and the thermal annealing protocol, the Na-SSZ-39 MMMs (Fig. 4B) possess antiaging properties. Although the aging characteristics may vary with film thickness, the self-standing 50 wt % Na-SSZ-39 MMM shows comparable CO_2-CH_4 selectivity and CO_2 permeability even 360 days after preparation (table S5). From an application point of view in the frame of CO_2 removal, this antiaging, high-flux, and high-selectivity membrane can allow substantial reductions in both operational and capital costs because a simplified and more energy-efficient operation scheme with less recycling and milder compression and recompression stages can be applied, in combination with reduced membrane areas and less replacement (*2*, *3*).

The gas-separation performance of the Na-SSZ-39 MMMs can thus be explained by a combination of three factors.

First, the selection of the Na-SSZ-39 zeolite as membrane filler is critical. Because of its accurate molecular size-sieving effect and strong CO_2-philicity, Na-SSZ-39 possesses enormous diffusivity and solubility selectivities, thus promoting ultrahigh mixed-gas selectivity. Moreover, the noncentrosymmetric AEI-type framework allows preparation of high–aspect ratio platelets. In contrast to many high–aspect ratio porous materials that possess 1D channels perpendicular to their base face (*41*, *42*), the SSZ-39 platelet is equipped with a 3D channel system, with 3.84-Å windows in its lateral face (Fig. 1B). Therefore, regardless of the platelet's orientation inside the membrane, the SSZ-39 pore system always allows unhindered gas flow (Fig. 4, D and E).

Second, the sudden jump in CO_2-CH_4 separation factor at 20 to 30 wt % loading suggests a percolation effect (Fig. 3A); from this loading onward, gas permeation through the membrane is predominantly going through the zeolite phase. The reason for this shift in phase dominance should be sought in the practical ability to incorporate ultrahigh loadings of the high–aspect ratio filler in the polymer. This creates a membrane morphology, which consists of a quasi-continuous zeolite phase across the membrane starting from only 20 to 30 wt % loading (Fig. 4D) and allows for percolation of the gas molecules with minimal influence of the less permeable polymer phase. The top and bottom views (Fig. 2F) of the MMMs show that the zeolite platelets pile up from the bottom

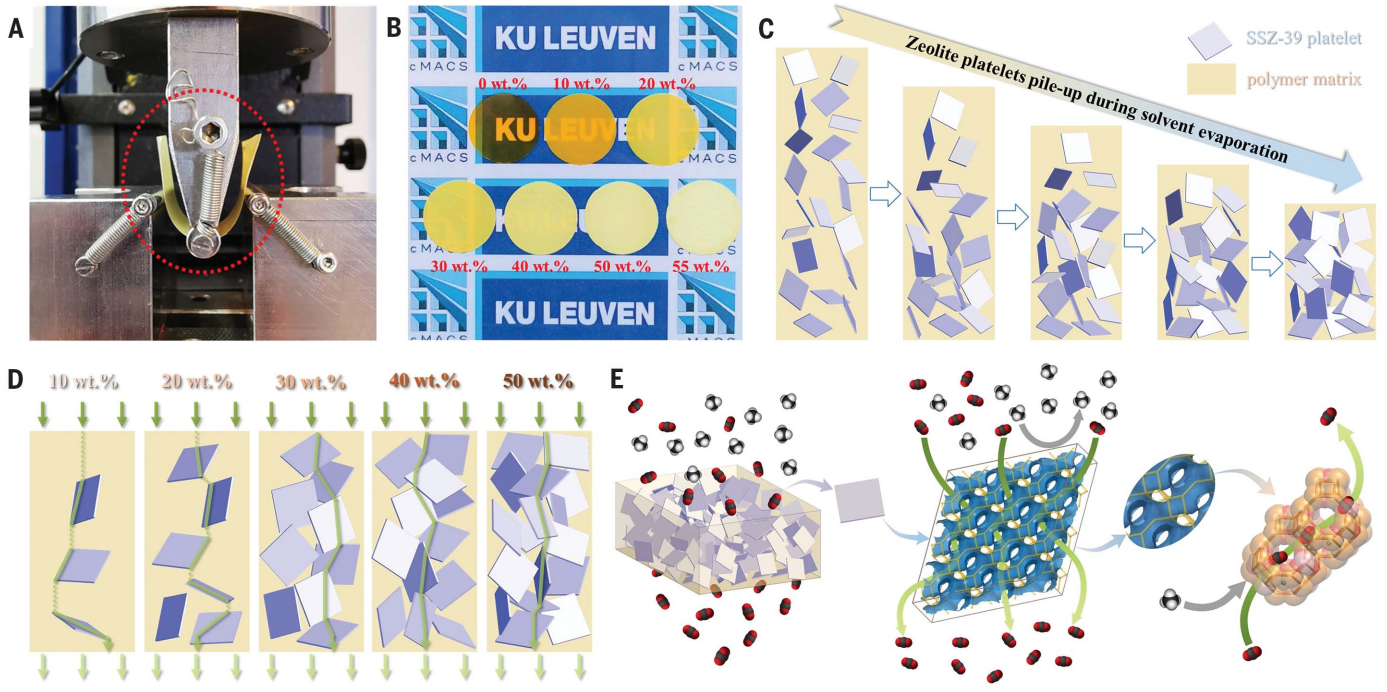

Fig. 4. Characterization and illustrations of platelet-shaped Na-SSZ-39 MMM. (**A**) The flexibility test (three-points bending) for 50 wt % Na-SSZ-39 MMM (table S4). (**B**) Visual appearance of 0 to 55 wt % Na-SSZ-39 MMMs. (**C**) Illustration of the solidification process of the platelet-shaped Na-SSZ-13 MMM, which results in a quasi-continuous zeolite phase across the membrane. (**D**) Illustration of the nonaligned zeolite platelet distribution in the polymer matrix with different zeolite loading. The preferential gas permeation pathways are indicated with the green arrows. (**E**) Schematic illustration of a MMM with (left) quasi-continuous zeolite phase and the unhindered CO_2 permeation (indicated with green arrows) through the (middle) 3D-channel system of platelet-shaped Na-SSZ-39 filler regardless of its orientation, as well as (right) the precise molecular sieving behavior that excludes CH_4 from CO_2 through the zeolite window.

and appear at the top of membrane when the zeolite loading reaches 30 wt % (Fig. 4C). In this context, the nonaligned, randomly oriented Na-SSZ-39 platelet distribution, which leads to a selective gas permeation highway, is a key driver and prerequisite for the membrane's extraordinary performance. This was also confirmed by comparing the platelet-shaped Na-SSZ-39 filler with a cuboid-shaped one [with similar properties except the aspect ratio (supplementary materials)]. As Fig. 3A shows, the sudden increment in CO_2-CH_4 selectivity was only observed for the platelet-shaped Na-SSZ-39 MMMs. Furthermore, although the cuboid-shaped Na-SSZ-39 MMMs also show great performances, the platelet-shaped Na-SSZ-39 MMMs exhibited far better CO_2-CH_4 selectivity and CO_2 permeability (tables S5 to S13), thus further confirming the morphology benefits of platelet-shaped Na-SSZ-39 MMMs.

Last, because the overall gas transport through the MMM is a net result of the properties of both zeolite and polymer, as well as of their mutual interactions, it is crucial to obtain a defect-free zeolite-polymer interface. Although rubbery polymers, such as polydimethylsiloxane (PDMS), facilitate creation of a defect-free interface (fig. S60), their intrinsically low selectivity and high permeability neutralize the beneficial contribution of the zeolite (table S15). The well-designed membrane preparation strategy minimizes the occurrence of unselective voids at the zeolite-Matrimid interface (figs. S54, S55, S58, and S59), allowing for ultrahigh zeolite loadings of >50 wt % without chemical modification of zeolite or polymer nor use of additives. Even at these high loadings, the Na-SSZ-39 MMMs still maintain desired flexibility (Fig. 4A), thus also creating excellent opportunities for module construction and upscaling.

Conclusions

We developed an ultrahigh-performance zeolite-filled MMM for CO_2 separations that shows unprecedented CO_2 removal performance, not only greater than that of any existing polymeric membrane or MMM but even surpassing that of most zeolite-only membranes. By circumventing the traditional incompatibility between zeolite filler and glassy polymer matrix, we prepared a flexible, defect-free zeolite-polyimide MMM with ultrahigh (>50 wt %) zeolite loadings. Na-SSZ-39 zeolite was discovered to be a superior filler because of its outstanding CO_2-philicity, precise molecular-sieving windows, strong competitive sorption behavior, and excellent stability, promoting strong, nonaging CO_2-separation performances. Because of the high–aspect ratio and 3D-channel system of the filler, a percolating gas permeation highway was created across the membrane, thus drastically enhancing the membrane's performance.

We used a scalable method to prepare defect-free zeolite-filled membranes with a commercially available glassy polymer, thus opening the door to developing well-processable, robust, and economical high-performance zeolite-filled MMMs for a variety of gas and liquid separations. It is especially beneficial for those zeolites that are difficult to be engineered into defect-free zeolite-only films.

REFERENCES AND NOTES

1. D. S. Sholl, R. P. Lively, *Nature* **532**, 435–437 (2016).
2. R. W. Baker, *Membrane Technology and Applications* (Wiley, ed. 3, 2012).
3. S. P. Nunes, K.-V. Peinemann, *Membrane Technology: In the Chemical Industry* (Wiley-VCH, ed. 2, 2006).
4. P. Bernardo, E. Drioli, G. Golemme, *Ind. Eng. Chem. Res.* **48**, 4638–4663 (2009).
5. R. W. Baker, B. T. Low, *Macromolecules* **47**, 6999–7013 (2014).
6. C. A. Scholes, G. W. Stevens, S. E. Kentish, *Fuel* **96**, 15–28 (2012).
7. S. Basu, A. L. Khan, A. Cano-Odena, C. Liu, I. F. J. Vankelecom, *Chem. Soc. Rev.* **39**, 750–768 (2010).
8. S. K. Simons, K. Nijmeijer, M. Wessling, *J. Membr. Sci.* **340**, 214–220 (2009).
9. G. He *et al.*, *Energy Environ. Sci.* **12**, 3305–3312 (2019).
10. M. E. Boot-Handford *et al.*, *Energy Environ. Sci.* **7**, 130–189 (2014).
11. L. M. Robeson, *J. Membr. Sci.* **320**, 390–400 (2008).
12. H. B. Park, J. Kamcev, L. M. Robeson, M. Elimelech, B. D. Freeman, *Science* **356**, eaab0530 (2017).
13. B. Comesaña-Gándara *et al.*, *Energy Environ. Sci.* **12**, 2733–2740 (2019).
14. N. Du *et al.*, *Nat. Mater.* **10**, 372–375 (2011).

15. M. Carta *et al*., *Science* **339**, 303–307 (2013).
16. H. W. H. Lai *et al*., *Science* **375**, 1390–1392 (2022).
17. Z. Lai *et al*., *Science* **300**, 456–460 (2003).
18. N. Rangnekar, N. Mittal, B. Elyassi, J. Caro, M. Tsapatsis, *Chem. Soc. Rev.* **44**, 7128–7154 (2015).
19. M. Y. Jeon *et al*., *Nature* **543**, 690–694 (2017).
20. X. Ma *et al*., *Science* **361**, 1008–1011 (2018).
21. N. Kosinov, J. Gascon, F. Kapteijn, E. J. M. Hensen, *J. Membr. Sci.* **499**, 65–79 (2016).
22. W. J. Koros, C. Zhang, *Nat. Mater.* **16**, 289–297 (2017).
23. S. Wang *et al*., *Energy Environ. Sci.* **9**, 1863–1890 (2016).
24. J. E. Bachman, Z. P. Smith, T. Li, T. Xu, J. R. Long, *Nat. Mater.* **15**, 845–849 (2016).
25. A. Kertik *et al*., *Energy Environ. Sci.* **10**, 2342–2351 (2017).
26. B. Wang *et al*., *Adv. Mater.* **32**, e1907701 (2020).
27. B. Seoane *et al*., *Chem. Soc. Rev.* **44**, 2421–2454 (2015).
28. J. Dechnik, J. Gascon, C. J. Doonan, C. Janiak, C. J. Sumby, *Angew. Chem. Int. Ed.* **56**, 9292–9310 (2017).
29. M. Galizia *et al*., *Macromolecules* **50**, 7809–7843 (2017).
30. I. F. Vankelecom, E. Scheppers, R. Heus, J. B. Uytterhoeven, *J. Phys. Chem.* **98**, 12390–12396 (1994).
31. R. Mahajan, R. Burns, M. Schaeffer, W. J. Koros, *J. Appl. Polym. Sci.* **86**, 881–890 (2002).
32. D. Bastani, N. Esmaeili, M. Asadollahi, *J. Ind. Eng. Chem.* **19**, 375–393 (2013).
33. S. I. Zones, Y. Nakagawa, S. T. Evans, G. S. Lee, US patent 5,958,370A (1999).
34. N. Nakazawa, S. Inagaki, Y. Kubota, *Chem. Lett.* **45**, 919–921 (2016).
35. M. Dusselier *et al*., *Chem. Mater.* **27**, 2695–2702 (2015).
36. M. Dusselier, M. E. Davis, *Chem. Rev.* **118**, 5265–5329 (2018).
37. Ch. Baerlocher, L. B. McCusker, Database of zeolite structures (2017); http://www.iza-structure.org/databases.
38. T. D. Pham, Q. Liu, R. F. Lobo, *Langmuir* **29**, 832–839 (2013).
39. S. Faramawy, T. Zaki, A. A. E. Sakr, *J. Nat. Gas Sci. Eng.* **34**, 34–54 (2016).
40. Y. Li *et al*., *Environ. Sci. Technol.* **53**, 11569–11579 (2019).
41. T. Rodenas *et al*., *Nat. Mater.* **14**, 48–55 (2015).
42. S. J. Datta *et al*., *Science* **376**, 1080–1087 (2022).

ACKNOWLEDGMENTS

We thank M. Roeffaers (KU Leuven, cMACS) for providing the Raman Spectromicroscopy measurement, M. Bastin for density measurement, and K. Yan for illustration drawing. This work was supported by the Fund for Scientific Research Flanders (FWO) and the Research Board of Ghent University (BOF). The computational resources (Stevin Supercomputer Infrastructure) and services used in this work were provided by the VSC (Flemish Supercomputer Center), funded by Ghent University, FWO, and the Flemish Government–department EWI. **Funding:** This work was supported by the Strategic Basic Research, Research Foundation–Flanders "SBOFWO" Biogas-Mambo S003721N (X.T. and I.V.); VlaioCataSPC moonrise HBC.2020.2612 (X.T. and I.V.); Research Foundation–Flanders "FWO" scholarships 1241822N, 12X7319N, and 1SB8821N (R.T., Y.L., and D.V.H.); Research Foundation–Flanders "FWO" G085220N (S.R., N.D.W., T.V.A., and M.D.); and Hercules fund AKUL/13/19 (I.V.) **Author contributions:** Conceptualization: X.T., Q.K., and I.V. Methodology: X.T., S.R., Q.K., R.T., M.D., and I.V. Investigation: X.T., S.R., Q.K., N.D.W., A.L., Y.L., I.A., D.V.H., and T.D. Visualization: X.T., S.R., A.L., and N.D.W. Funding acquisition: I.V., M.D., T.V.A., and V.V.S. Project administration: X.T. and I.V. Supervision: I.V. Writing – original draft: X.T. and R.T. Writing – review and editing: All authors. **Competing interests:** The authors declare that they have no competing interests. X.T., I.V., M.D., S.R., and R.T. submitted patent application EP22170367.1 by KU Leuven, which is based on this invention. **Data and materials availability:** All data are available in the main text or the supplementary materials.

SUPPLEMENTARY MATERIALS

science.org/doi/10.1126/science.ade1411
Materials and Methods
Supplementary Text
Figs. S1 to S66
Tables S1 to S21
References (*43–191*)
Movies S1 and S2
Data S1

Submitted 27 July 2022; accepted 16 November 2022
10.1126/science.ade1411

Truly combining the advantages of polymeric and zeolite membranes for gas separations

Xiaoyu TanSven RobijnsRaymond ThürQuanli KeNiels De WitteAran LamaireYun LiImran AslamDaan Van HavereThibaut DonckelsTom Van AsscheVeronique Van SpeybroeckMichiel DusselierIvo Vankelecom

Science, 378 (6625), • DOI: 10.1126/science.ade1411

Material design maximizes performance

Zeolites are able to separate molecules with similar size and shape because of their well-defined, uniform pore size and specific adsorption properties. However, it has been a challenge to retain these features when blending a zeolite with a polymeric matrix support. Tan *et al*. developed a method to put high loadings of the aluminosilicate SSZ-39, which is known for its attraction of carbon dioxide, into a commercial polyimide selected for its compatibility with the zeolite. The resulting mixed matrix membranes were flexible and defect free, showing excellent separation of carbon dioxide that even exceeded the performance of pure zeolite membranes. —MSL